Simulation and Measurement Validation of a Finite-Length Cylindrical 3D UTD Model

RUWEI LIU[1], YI GONG [1] (Senior Member, IEEE), SOFIE POLLIN [2], AND YANG MIAO [2,3] (Member, IEEE)

[1]Department of Electrical and Electronic Engineering, Southern University of Science and Technology, Shenzhen 518055, China

[2]Faculty of Electrical Engineering, Katholieke Universiteit Leuven, 3000 Leuven, Belgium

[3]Faculty of Electrical Engineering, University of Twente, 7514 AW Enschede, The Netherlands

CORRESPONDING AUTHOR: Y. MIAO (e-mail: y.miao@utwente.nl)

ABSTRACT In this paper we provide a modified 3D Uniform Theory of Diffraction (UTD) model for a finite-length cylinder, and validate the model by comparing to the simulation and the measured data. The presented finite-cylinder UTD model is adapted from the conventional infinite-cylinder model, and we additionally add edge diffraction occurring at the edge of the cap of the finite cylinder. The simulation reference is obtained from the CST simulation and the measurement reference is obtained from a vector network analyzer based channel sounder. From the numerical examples and analysis, it is shown that the modified model agrees well with the references and is more accurate than the conventional unmodified model. This study proves the importance of the edge diffraction field for finite-cylinder UTD solutions specially when 1) the transmitter and receiver are at different heights relative to the cylinder, and 2) one is below and the other is above the height of the cylinder.

INDEX TERMS Uniform theory of diffraction (UTD), finite-length cylindrical model, geometry optics (GO), electromagnetic scattering, edge diffraction.

I. INTRODUCTION

WITH the deployment of 5G cellular networks and the commencement of 6G research [1], [2], along with the rapid development of other wireless technologies such as Wi-Fi [3], wireless communication infrastructures and systems become more capable of providing even higher speed and even lower latency for wireless connectivity. Towards-6G, millimeter-wave (mmWave) and sub-THz frequency bands [4] are envisioned to dominate, due to the availability of large bandwidth spectrum, providing more frequency resources for even larger throughput. In the same while, with higher frequencies (naturally higher free space path loss) and smaller wavelength, the cells tend to be densified and could be easily affected by moving vehicles/machines or humans [5], regardless of outdoor or indoor application scenarios. The obstruction or blockage of a communication link by machines/vehicles or humans could degrade the communication performance and could

also result in inaccurate localization performance. Hence, a deterministic, accurate yet simple/fast model is needed to represent the influence of machines/vehicles/humans - finite geometry with dielectric and conductivity properties - on the radio waves, so that we could predict the influences and take countermeasures.

With the support of advanced computer technology and hardware, computational electromagnetics [6], [7] has become an important branch of electromagnetism to solve electromagnetic problems, such as the approximate solutions to Maxwell's equations to calculate the antenna performance, electromagnetic compatibility, radar cross section and radio wave propagation. Computational electromagnetic methods can be categorized into the rigorous full-wave method such as the integral equation solvers (e.g., Method of Moments [8]), the differential equation solvers (e.g., Finite-difference time-domain [9], Finite Element Method [10], Finite Integration Technique [11]),

as well as the high frequency approximation methods (e.g., Physical Optics (PO) [12], [13], Geometry Optics (GO) [14], Uniform Theory of Diffraction (UTD) [15], [16]). For the rigorous numerical approaches, the induced currents by source are determined by a large set of linear equations hence may be extremely time-consuming. Considering the computation time/efficiency, accuracy, and application condition, the approximation solutions to Maxwell's equations could be suited for modeling the interactions between machine/vehicle/human and radio waves for 3D deterministic modeling and electromagnetic field computation in dynamic channel conditions.

Among the high frequency approximation approaches, approximation in PO is made when determining the surface currents. References [7], [17], [18] The geometry surface is divided into meshes that are much smaller compared to the wavelength and each mesh is considered as locally planar where reflection occurs according to GO. Instead of using Maxwell's equations that gives us the solution at any point in space, PO approach is used where it only gives solution in the lit region. The advantage of using PO is that it has wide applicability for differently shaped scatters, and it costs less computation time. PO gives a good approximation of the electromagnetic field when applying to high frequency and low curvature scenarios. A high frequency approximation method indicates that the surface of an object is much larger than the wavelength of the impinging wave. Originally, PO was developed for analyzing scattering from a perfect electric conductor (PEC) material, but the concept of approximating currents is quite general and applicable for magnetic conductors, dielectric materials, and bodies with surface impedance, etc. The major source of errors in the PO method is at the edge of surface, or when the surface curvature of surface is large and multiple reflections exists.

Approximation approaches of GO is based on the ray theory of electromagnetic field propagation [19], [20]. The concepts of ray and ray tube are used to analyze scattering and energy propagation. Its physical concept is clear and easy to calculate. However, GO can only study the problems of direct (incident), reflection and refraction. When a GO ray encounters surface discontinuities, such as edges, spires, or grazing incidence on a surface, it will produce a shadow region that it cannot enter. Geometry theory of diffraction and UTD is developed from Geometrical Optics (GO), it introduced a concept of diffracted ray. The diffracted ray penetrate into both the shadow and lit zones, and thereby overcome the failure of GO in the shadow region.

These approximation solutions to Maxwell's equations need less computation time compared to the rigorous full wave solutions, but at the cost of generality in particular the GO and UTD. as it can be applied only to canonical shapes (in the presented form). The Authors should focus on the specific strengths of semi-analytical techniques as being able to reveal hidden physical phenomena. UTD has the unique advantages of small required computing space and high computing speed. In particular, the commonly used CST

Studio Suite 3D Electromagnetics (EM) simulation and analysis software use Integral Equation Solver for the simulation in electrically large occasions.

Based on above revelation, UTD could be suited for the modeling of the interactions between machine/vehicle/human and radio waves, because their efficiency and decent accuracy for 3D deterministic modeling and electromagnetic field computation. In early development of UTD, scatterers studied were usually PEC. In the literature, a lot of work has been done for studying the problem of non-perfectly-conducting project [21]–[23]. Depending on the target object, PEC is a reasonable approximation for good metallic conductors.

In wireless body area network (WBAN) [24]–[27] and human body shadowing [28] studies, there have been ample examples on using UTD for accurate modeling of human body impact on wireless communications. These works on the human body shadowing effects using UTD are mostly carried out in 2D space when transmit antenna (TX) and receive antenna (RX) are at the same height. The investigations in [29], [30] on the 3D UTD cylindrical model show the defect of ignoring the edge diffraction field on the total received field, it means, for a finite 3D cylinder, the top/bottom of cylinder diffracted field have an influence on the total field for single-cylinder scattering problem.

In this paper, we propose a modified 3D UTD model for a finite PEC circular cylinder. The modification is based on the conventional model presented in literature [25], [26] which have ignored the edge diffraction. We integrate in the modified model the edge diffraction which occurs when EM waves impinge on the cap edge for single-cylinder scattering and thus influence the total received field. The modified and unmodified UTD models are compared with the CST simulation and measurement references. By comparing various elevation and azimuth angles, we validate the importance of integrating edge diffraction especially when the RX is above the top of the cylinder while TX is below it (or vice versa). In addition, UTD calculation is significantly faster than numerical simulation using the CST Integral Equation Solver. The modified UTD model is based on the model of E. Plouhinec in [29] and [30], the contribution of edge diffraction field value is not considered in the previous model, it works well in most of its scenarios but highlights the fact that the top and bottom disks cylinder diffracted fields have an influence on the total received field for the presented single cylinder problem, and our modified model integrating the edge diffraction contribution at the cap of cylinder. The validation proves the importance of edge diffraction especially when one of the TX/RX is higher than finite cylinder.

In Section II, the 3D UTD models for an infinite and a finite cylinder are described respectively, we focus on the 3D GO ray-tracing and the UTD formulations used for computing the electromagnetic field. In Section III and IV we describe the simulation campaign and focus on the validation of the electric field calculation by the modified UTD, making a comparison between the modified UTD and the CST simulation result. In Section V we describe the measurement
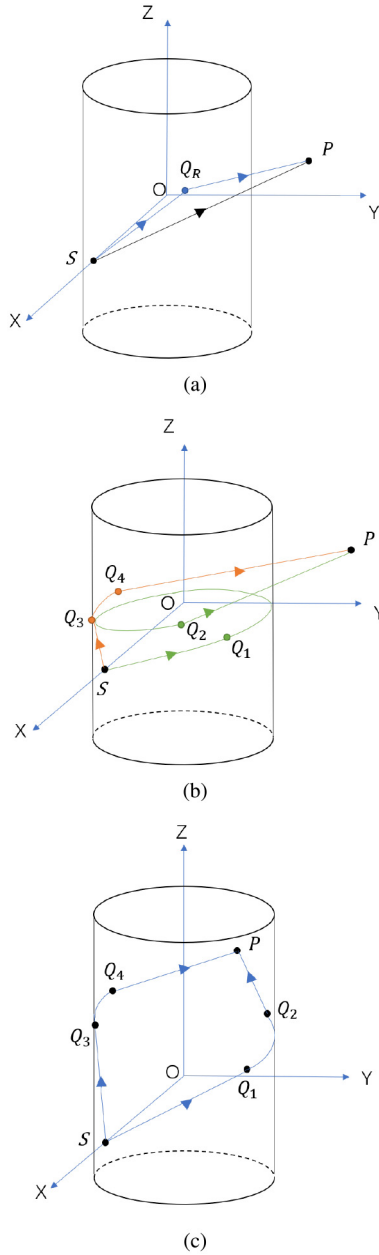
(a)

(b)

(c)

FIGURE 1. Infinite cylinder ray-tracing scenario for (a) and (b) in LOS scenario, and (c) in NLOS scenario.

campaign, and VI focus on the validation of channel calculation by the modified UTD, making a comparative analysis on the modified UTD, the CST simulation and the measurement channel results.

II. 3D UTD MODEL FOR FINITE-LENGTH CYLINDER
A. RECAP - MODEL FOR INFINITE CYLINDER
Referring to Figure 1, we first look at the composition of GO rays existing between the source point S and the receiver point P in presence of a circular cylinder with infinite length. We could have two ray-tracing scenarios for this 3D infinite cylinder: P in the Line Of Sight (LOS) and in the Non Line Of Sight (NLOS). As is also shown in Figure 2, the LOS
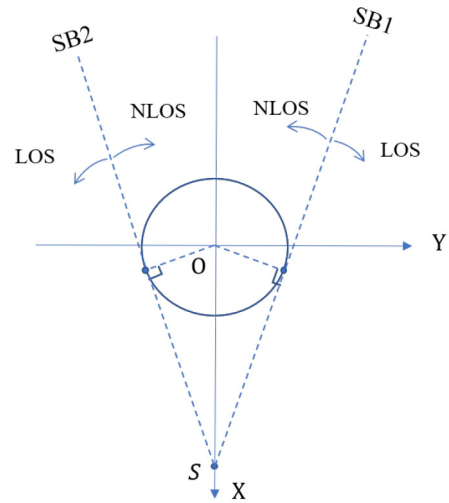

FIGURE 2. Top view for infinite cylinder.

and NLOS are separated by the shadow boundary SB_1 and SB_2. For LOS scenario, there are three rays as shown in Figure 1 (a) and (b): one direct ray (in black), one reflected ray (in blue) and two surface diffracted rays (in orange and green). For NLOS scenario, there are two surface diffracted rays (in blue) as shown in Figure 1 (c). Note that all the ray paths are deduced from Fermat's principle.

Note that the field expressions are defined below, some parameters in the following formulas are not defined due to space limitation and can be found in the *Appendix*.

1) DIRECT FIELD
Direct field corresponds to free space propagation, and signal propagates directly from S to P in this case. The direct field at P is $\vec{E}^i(P)$ expressed as [15]:

$$\vec{E}^i(P) = \vec{E}_0 \cdot \frac{e^{-jks}}{s}, \tag{1}$$

where s is the shortest distance between S and P, and $\vec{E}_0$ is the emitted field generated by S related with the antenna pattern.

2) REFLECTED FIELD
The reflection occurs on the surface of objects, and the surface acts as a mirror. The reflected field at P is $\vec{E}^r(P)$ expressed as [15]:

$$\vec{E}^r(P) = \vec{E}^i(Q_R) \cdot \overline{\overline{R}} \cdot A^r \cdot e^{-jks_r}, \tag{2}$$

where s_r is the path length from the reflection point Q_R to P. The A^r indicates the spreading factor for incident wave depend on surface geometry which is expressed as:

$$A^r = \sqrt{\frac{\rho_1{}^r \rho_2{}^r}{(\rho_1{}^r + s^r)(\rho_2{}^r + s^r)}}. \tag{3}$$

$\overline{\overline{R}}$ is the Fresnel dyadic reflection coefficient (dyadic operation is performed between the vectors), it's a matrix

expressed as:

$$\overline{\overline{R}} = R_s \vec{e}_\perp \vec{e}_\perp + R_h \vec{e}_\parallel^i \vec{e}_\parallel^r. \tag{4}$$

The reflection coefficients $R_{s,h}$ can be written as:

$$R_{s,h} = -\sqrt{\frac{-4}{\xi^L}} \cdot \left\{ \frac{e^{-j\pi/4}}{2\xi^L\sqrt{\pi}} \left[1 - F\left(X^L\right)\right] + \vec{P}_{s,h}\left(\xi^L\right) \right\} \tag{5}$$

Please refer to the Appendix for further definitions.

3) SURFACE DIFFRACTED FIELD

The surface diffraction occurs on the smooth surface of cylinder, and the rays creep on the cylinder. The diffracted field is expressed as [15]:

$$\vec{E}_{1,2}^{sd}(P) = \vec{E}^i\left(Q_{1,3}\right) \cdot \overline{\overline{T}} \cdot A^{sd} \cdot e^{-jks^d}. \tag{6}$$

The Q_1 and Q_3 are the attachment points, Q_2 and Q_4 are the detachment points. The ray of Q_1 and Q_2 (resp. Q_3 and Q_4) will be called ray1 (resp. ray2). s^d is the path length from Q_2 (resp. Q_4) to P. The $\vec{E}_1^{sd}(P)$ (resp. $\vec{E}_2^{sd}(P)$) corresponds to ray1 (resp. ray2). The A^{sd} indicates the spreading factor for incident wave depend on surface geometry. A^{sd} is expressed as:

$$A^{sd} = \sqrt{\frac{\rho_2^d}{s^d\left(\rho_2^d + s^d\right)}}. \tag{7}$$

$\overline{\overline{T}}$ is the Fresnel dyadic transfer coefficient (dyadic operation is performed between the vectors), and is a matrix expressed as:

$$\overline{\overline{T}} = T_s \vec{b}_1 \vec{b}_2 + T_h \vec{n}_1 \vec{n}_2. \tag{8}$$

Please refer to the Appendix for further definitions.

4) TOTAL FIELD

The total field for infinite cylinder can be expressed as:

$$\vec{E}_{total}(P) = \alpha\left(\vec{E}^i(P) + \vec{E}^r(P)\right) + \sum_{i=1}^{2} \vec{E}_i^{sd}(P), \tag{9}$$

where $\alpha = 1$ (resp. $\alpha = 0$) is the LOS (resp. NLOS) case. LOS and NLOS are separated by shadow boundaries as shown in Figure 2. If we set $S(\rho', 0, 0)$ and $P(\rho, \theta, \phi)$, and the radius of the cylinder to be r_{cyl}, the shadow boundary SB_1 and SB_2 in Figure 2 can be calculated by:

$$SB_1 = \arccos\frac{r_{cyl}}{\rho \cdot \sin\theta} + \arccos\frac{r_{cyl}}{\rho'}, \tag{10}$$

$$SB_2 = 2\pi - \left(\arccos\frac{r_{cyl}}{\rho \cdot \sin\theta} + \arccos\frac{r_{cyl}}{\rho'}\right). \tag{11}$$

B. MODIFIED MODEL FOR FINITE CYLINDER

The studies in [29], [30] have clearly indicated that the direct, reflected and surface diffracted field are not enough to describe the electric field for finite cylinder when the position of the receiving point is higher than the top of the cylinder. Therefore, in this paper, we revise the 3D UTD model to take the edge diffracted field into account.
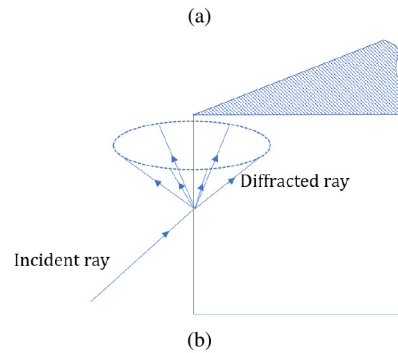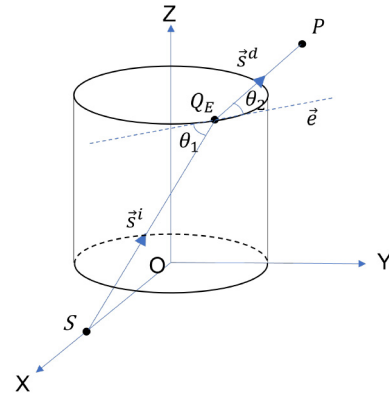

FIGURE 3. Edge diffracted ray: (a) edge diffracted ray on a finite cylinder, (b) a cone of edge diffracted rays.

1) DIRECT, SURFACE DIFFRACTED AND REFLECTED FIELD

The expressions for these three fields are the same as above and its supplementary definitions in the Appendix. But for a finite-length cylinder, LOS and NLOS can no longer be defined on the 2D plane but should be on the 3D space, which can be calculated by ray tracing method [31], [32]. The direct ray is present if P is in LOS and absent in NLOS. The reflected ray is present (resp. absent) if Q_R is on (resp. not on) the cylinder. The surface diffracted ray is present (resp. absent) if attachment point and detachment point is on (resp. not on) the cylinder.

2) EDGE DIFFRACT FIELD

Edge diffraction occurs when an electromagnetic wave is incident on the edge. The angle between the edge diffracted ray and the edge (θ_2 in Figure 3(a)) should be equal to the angle between the corresponding incident ray and the edge (θ_1 in Figure 3(a)). An incident ray can excite numerous diffracted rays, which are all located on a conical surface with the diffracted point as the fixed point as shown in Figure 3(b). For a finite cylinder, there would be edge diffraction which occurs at the cap edge of the cylinder as is shown in Figure 3, its range covers a part of LOS and NLOS and can be found by ray tracing method [31], [32].

For S and P at fixed positions, the diffracted point Q_E and diffracted rays can be searched by the numerical method of ray tracing. The position of Q_E needs to satisfy the following

equation:

$$\vec{e} \cdot \vec{s}^i = \vec{e} \cdot \vec{s}^d \tag{12}$$

where $\vec{e}$ is the unit vector of the edge incident point Q_E at the edge tangent, $\vec{s}^i$ and $\vec{s}^d$ are the unit vectors of the incident and diffracted ray respectively.

The edge diffracted field is expressed as [16]:

$$\vec{E}_{\theta,\phi}^{ed} = \vec{E}_{\theta,\phi}^i \cdot \overline{\overline{D}}(f_c) \cdot A^{ed} \cdot e^{-jks_d}. \tag{13}$$

The A^{ed} indicates the spreading factor for incident wave depend on surface geometry. A^{ed} is expressed as:

$$A^{ed} = \sqrt{\frac{\rho}{s(\rho + s)}} \tag{14}$$

ρ is the edge caustic. s is the shortest distance between Q_E and P. The dyadic diffraction coefficient $\overline{\overline{D}}$ (dyadic operation is performed between the vectors) can be written as:

$$\overline{\overline{D}} = -D_s \vec{\beta}_0' \vec{\beta}_0 - D_h \vec{\phi}' \vec{\phi}. \tag{15}$$

Please refer to the Appendix for further definitions.

3) TOTAL FIELD

The proposed modified total field for a finite-length cylinder can be expressed as:

$$\vec{E}_{total}(P) = \alpha \left(\vec{E}^i(P) + \beta_r \vec{E}^r(P) \right)$$
$$+ \beta_{sd}^i \sum_{i=1}^{2} \vec{E}_i^{sd}(P) + \beta_{ed}^i \sum_{i=1}^{n} \vec{E}_i^{ed}(P), \quad \tag{16}$$

where $\alpha = 1$ (resp. $\alpha = 0$) indicates the LOS (resp. NLOS) case; $\beta_r = 1$ (resp. $\beta_r = 0$) if Q_r is on the cylinder (resp. absent); $\beta_{sd}^i = 1$ (resp. $\beta_{sd}^i = 0$) if i^{th} surface diffracted ray is present (resp. absent); $\beta_{ed}^i = 1$ (resp. $\beta_{ed}^i = 0$) if i^{th} edge diffracted ray is present (resp. absent).

III. FIELD VALIDATION OF THE MODIFIED 3D UTD MODEL VIA SIMULATION
A. CST SIMULATOR
To verify the modified UTD model, we will first compare the UTD results with EM simulation. The CST-Microwave studio is used to get the simulation result. The CST program is high-performance 3D EM analysis software package for analyzing and optimizing EM components, and we use the integral equation solver to get the results. The integral equation solver is a 3D full-wave solver, based on the Method of Moments (MOM) technique with Multi-Level Fast Multipole Method (MLFMM). The integral equation solver uses a surface integral technique, which makes it much more efficient than full volume methods when simulating electrically large scenarios.
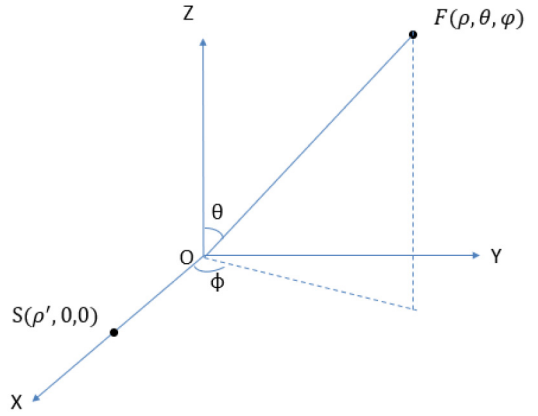

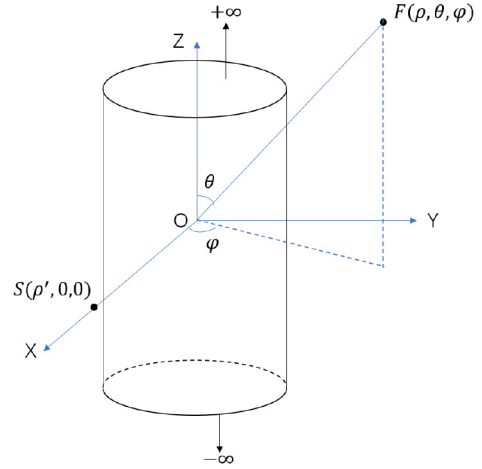FIGURE 4. LOS (free space) scenario to validate the direct field.

FIGURE 5. Infinite cylinder scenario to validate the reflected and surface diffracted field.

B. FIELD VALIDATION
For this comparison, we use the UTD and CST simulation results to validate the calculation in presence of a PEC cylinder of radius $r = 2\lambda$. The measurements were made at frequency $f = 5$ GHz. The simulation were carried out with reference to a spherical coordinate system (ρ, θ, ϕ). To simplify the calculation, we set $S(\rho', 0, 0)$ and $P(\rho, \theta, \phi)$. The transmit/receive antennas used in the simulation and calculation are both a typical horn antenna working from 4 GHz to 5 GHz.

We use Normalized Mean Square Error (NMSE) to quantify the discrepancy between the UTD calculated field and the CST simulated field, and is defined as:

$$\text{NMSE} = \frac{\sum \left(|\vec{E}_{CST}| - |\vec{E}_{UTD}| \right)^2}{\sum |\vec{E}_{CST}|^2} \tag{17}$$

where $|\vec{E}_{CST}|$ and $|\vec{E}_{UTD}|$ are the amplitude of the E-field calculated by the CST and the modified UTD respectively.

C. VALIDATE THE DIRECT, REFLECTED, AND SURFACE DIFFRACTED FIELDS
We want to first validate the direct field in the free space scenario without cylinder as is shown in Figure 4. The results
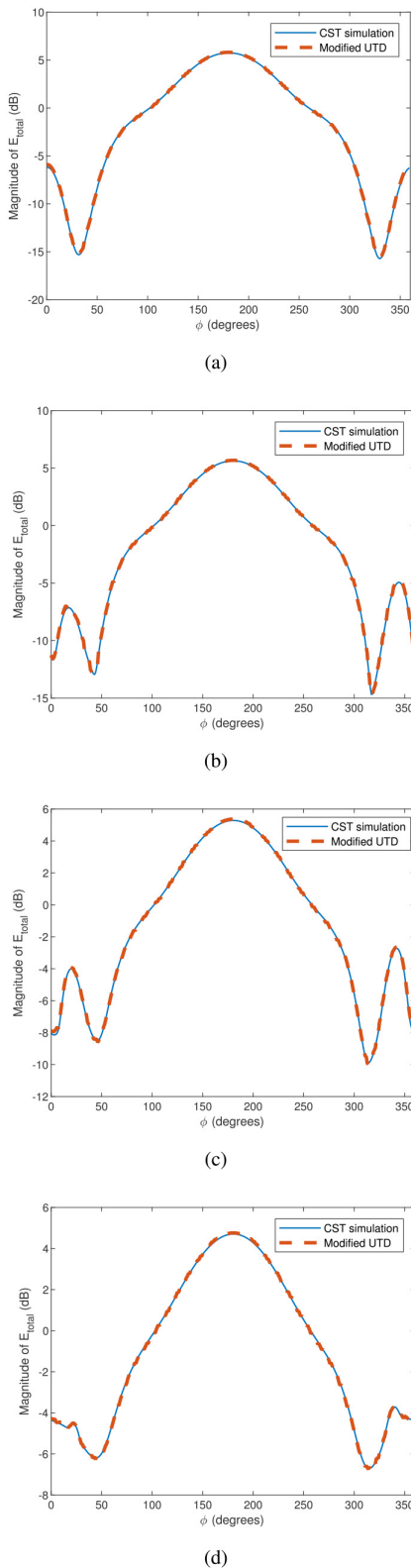
(a)

(b)

(c)

(d)

FIGURE 6. LOS scenario results of UTD and CST simulation, at (a) $\theta = 90°$, (b) $\theta = 80°$, (c) $\theta = 70°$, (d) $\theta = 60°$ for $f = 5$ GHz, $\rho' = 10\lambda$, $\rho = 20\lambda$.

are shown in Figure 6; from visual inspection we notice a good agreement between simulation and calculation. The NMSE between the direct field by UTD and that by CST
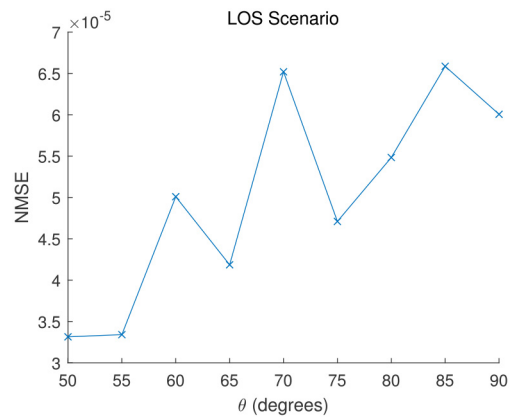

FIGURE 7. NMSE between results of the modified UTD and the CST for LOS scenario.

is shown in Figure 8, where the result error is negligible (NMSE$< 7 \times 10^{-5}$).

We then want t validate the reflected and surface diffracted field in this infinite-cylinder scenario considering a long PEC cylinder as is shown in Figure 5. The total field is composed of $\vec{E}^i$, $\vec{E}^r$ and $\vec{E}^{sd}$, and $\vec{E}^{ed}$ is neglected and will be verified in next step. The results are shown in Figure 7. Overall, the trend of the two results is consistent. It can be seen that the error is a litter larger for $\phi \in [0°, 50°]$, $[310°, 360°]$ and around $[170°, 190°]$ in NLOS. And the overall error increases slightly with the decrease of θ. For $\phi \in [0°, 50°]$, $[310°, 360°]$, $\beta_{sd} = 0$. The NMSE is shown in Figure 9. With the decrease of θ, the value of NMSE decreases slightly, but it changes little on the whole ($NMSE < 7.5 \times 10^{-3}$), which means our modified UTD could predict the direct, reflected and surface diffracted fields very well.

D. VALIDATE FINITE CYLINDER SCENARIO & EDGE DIFFRACTION

For this scenario, the results are presented in the case of the PEC finite cylinder as is shown in Figure 10. The length of the cylinder on the positive half of z-axis is $h = \lambda$ and is long in the negative half of z-axis. The results are shown in Figure 11.

When $\theta = 90°$, there is no $\vec{E}^{ed}$ at NLOS ($\phi \in [162°, 198°]$) for the modified UTD, so the $\vec{E}_{total}$ of modified UTD is the same as the unmodified UTD without $\vec{E}^{ed}$, however, the CST results of Figure 11 (a) changes significantly compared with Figure 8 (a). Comparing the scenarios ($\theta = 90°$) correspondingly in the 2 figures, obviously the difference stems from the top surface of cylinder. One sensible guess would be that the multi-order edge diffraction occurs at the top of cylinder which is not included in the modified nor the unmodified models. Moreover, in LOS the result of modified UTD and unmodified UTD without $\vec{E}^{ed}$ is similar as the value of $\vec{E}^{ed}$ is small.

When $\theta = 80°$, we can observe the discontinuity of $\vec{E}_{total}$ in the unmodified UTD without $\vec{E}^{ed}$, when the direct ray is blocked by the cylinder and there is no $\vec{E}^r$ or $\vec{E}^{sd}$ judged
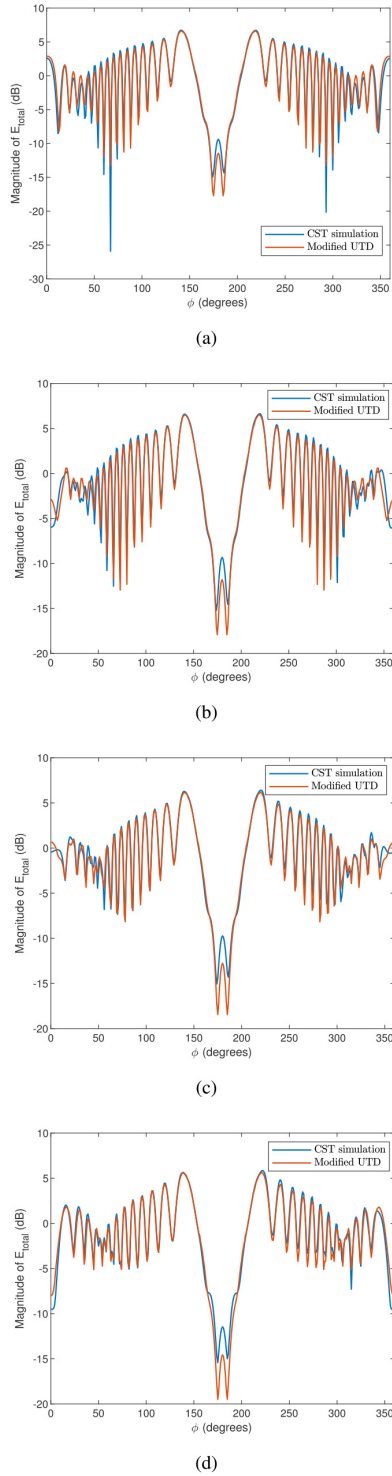
(a)

(b)

(c)

(d)

FIGURE 8. Infinite cylinder scenario results of UTD and CST simulation, at (a) $\theta = 90°$, (b) $\theta = 80°$, (c) $\theta = 70°$, (d) $\theta = 60°$ for $f = 5$ GHz, $\rho' = 10\lambda$, $\rho = 20\lambda$.

FIGURE 9. NMSE between the modified UTD and the CST for infinite cylinder scenario.
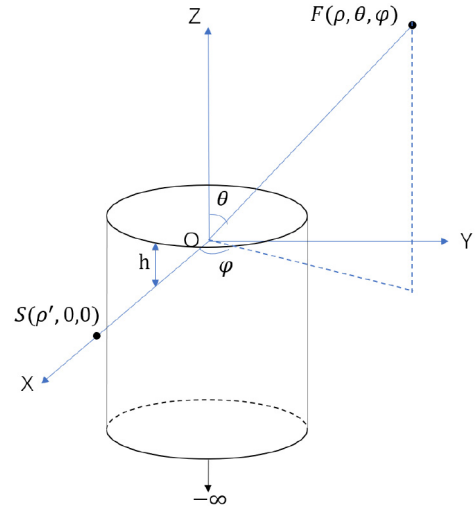
FIGURE 10. Finite cylinder scenario.

between rays and hence suggesting the edge diffraction must be considered in the model.

The NMSE of the modified UTD and the unmodified UTD without $\vec{E}^{ed}$ are shown in Figure 12. The reference value is the CST simulation results. For all angles, the NMSE of modified UTD is smaller compared to the unmodified UTD without $\vec{E}_{ed}$. It is observed that the NMSE is larger at around $\theta = 85°$, in this region, the receiving point is located around the shadow boundary (determined by the transmitting point and the top edge of the cylinder), and the main error occurs in NLOS, which suggests other radiation mechanisms such as multi-order diffraction is nonnegligible especially in NLOS. When the receiving point is much higher ($\theta \leq 80°$), the direct field is the main contribution of the total field, and the error is small.

IV. CHANNEL VALIDATION OF THE MODIFIED 3D UTD MODEL VIA MEASUREMENT
A. MEASUREMENT CAMPAIGN
The measurement was carried out in the corridor in the building of the College of Engineering, South University of

by (16), but the result of the modified UTD could maintain the continuity.

And for $\theta \leq 80°$, $\vec{E}_{total}$ of the modified UTD contains $\vec{E}^i$ and $\vec{E}^{ed}$, while the E_{total} of UTD without $\vec{E}^{ed}$ only contain $\vec{E}^i$. We can notice an oscillatory behavior of the CST and modified UTD results, which implying the interference
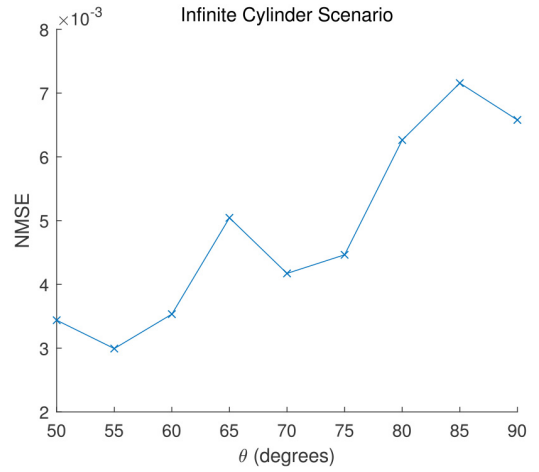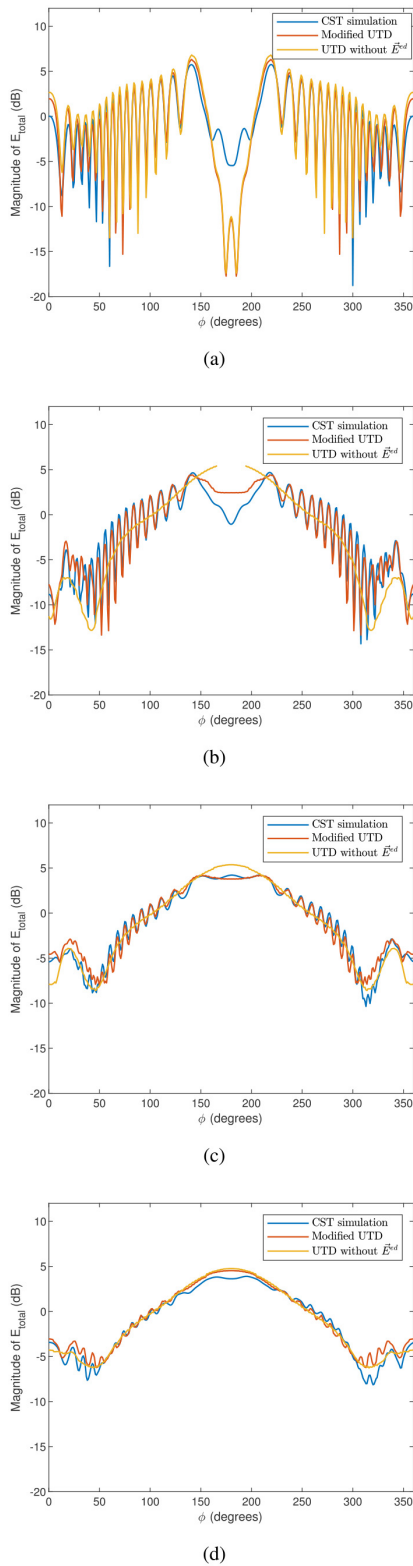
(a)

(b)

(c)

(d)

FIGURE 11. Finite cylinder scenario results of the proposed modified UTD, the unmodified UTD and the CST simulation, at (a) $\theta = 90°$, (b) $\theta = 80°$, (c) $\theta = 70°$, (d) $\theta = 60°$ for $f = 5$ GHz, $h = \lambda$, $r = 2\lambda$, $\rho' = 10\lambda$, $\rho = 20\lambda$.

Science and Technology, as is shown in Figure 13. The tested cylinder is a thick and hollow stainless steel. The radius of cylinder $r = 0.19$ m and height $H = 1.17$ m. The distance
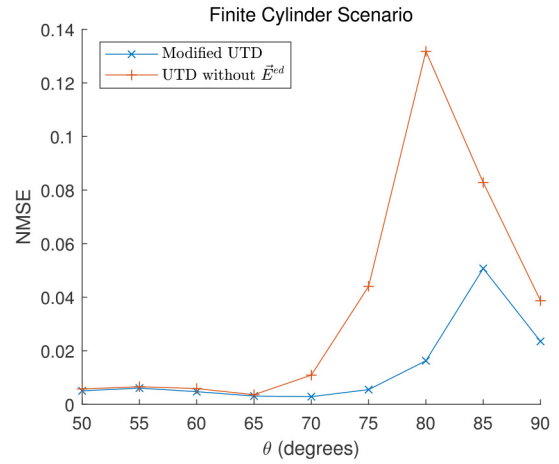

FIGURE 12. NMSE between the modified UTD and the unmodified UTD without $\bar{E}^{ed}$, respectively, with CST for finite cylinder scenario.

FIGURE 13. Channel measurement scenario.

between the tested cylinder/antennas and the sidewalls is at least 1 m.

We used the same rectangular horn antennas for both TX and RX to provide directive radiation pattern and avoid the interference of multipath. The working frequency band of the antenna is 2.17 GHz to 3.3 GHz with a gain of 13 dBi. The orientations of TX and RX were always in parallel to the ground and pointing to the cylindrical axis to avoid interacting with the walls.

The measurements were performed at $f = 2.25$ GHz. The measurements were carried out with reference to the cylindrical coordinate system (ρ, ϕ, z). To simplify the calculation, we set TX$(\rho', 0, 0)$ and RX(ρ, ϕ, Z_{RX}), and $\rho' = \rho = 2$ m for our measurement. The height of the top surface of the cylinder is denoted as h; it means that the height difference between the top of the cylinder and the center of TX is h. In the measurements, $\phi \in [0°, 360°]$ is with a 10° step sweep. The measurement setup is shown in TABLE 1.

B. NUMERICAL RESULTS - CHANNEL VALIDATION

The measurement results, the corresponding CST simulated results, and the unmodified UTD results are shown in comparison to the proposed modified UTD results in Figure 14.
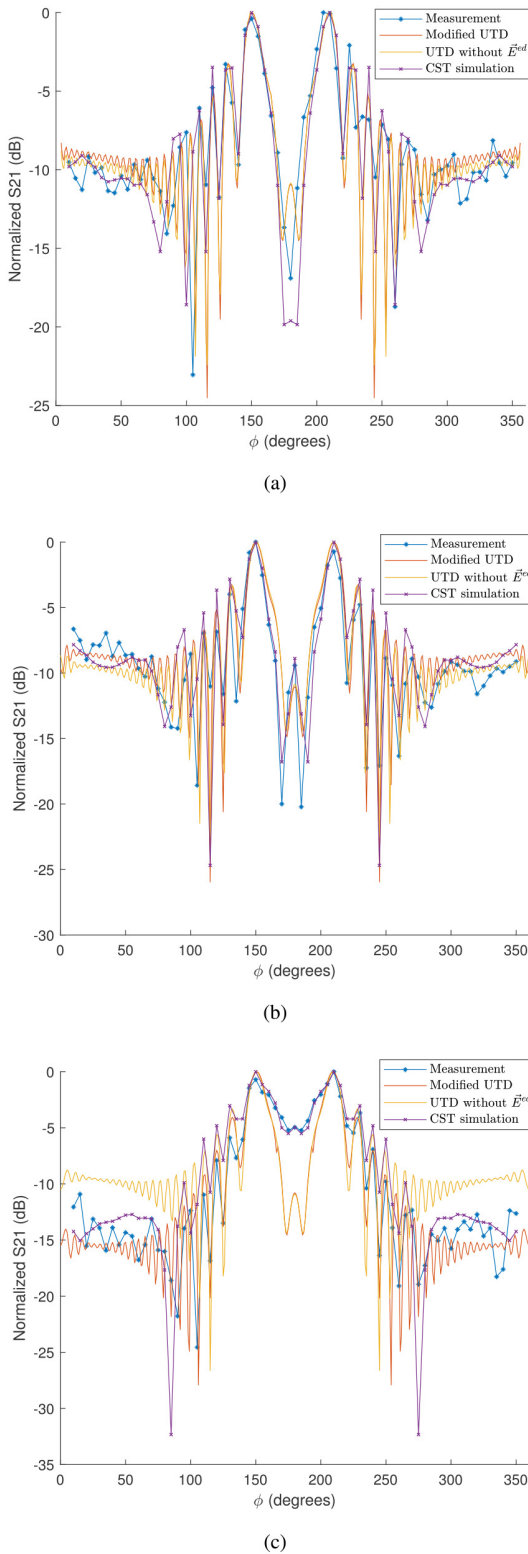
(a)

(b)

(c)

FIGURE 14. Comparison of the normalized channels between the proposed modified UTD, the unmodified UTD, the CST simulation and measurement references for (a) scenario 1 in Table 1, (b) scenario 2, and (c) scenario 3, where $r = 0.19m$, $\rho' = 2m$, $\rho = 2m$.

In Figure 14 (a) and (b), the UTD results and the measurement results agree well; the gap between the modified and the unmodified UTD model is small because the contribution

TABLE 1. Measurement setup.

	RX height $Z_{RX}(m)$	Top of cylinder height $h(m)$
Scenario 1	0	0.39
Scenario 2	0.27	0.39
Scenario 3	0.475	0.25

TABLE 2. NMSE comparison.

	NMSE		
	Modified UTD	UTD without $\vec{E}^{ed}$	CST
Scenario 1	2.69×10^{-2}	2.77×10^{-2}	3.47×10^{-2}
Scenario 2	4.41×10^{-2}	4.76×10^{-2}	5.16×10^{-2}
Scenario 3	6.22×10^{-2}	12.26×10^{-2}	4.11×10^{-2}

TABLE 3. Calculation time.

	CST simulation	UTD calculation
Scenario 1	4830s	3.9s
Scenario 2	5254s	3.9s
Scenario 3	4958s	4s

of edge diffraction field is small when the RX is lower than the cylinder top.

When it comes to Figure 14 (c), there is a big gap between the modified and the unmodified UTD models, because the edge diffraction field contributes more than that in (a) and (b), and it is obvious that the results of the modified UTD are in better agreement with the measurement results. There is significant gap of UTD in NLOS ($\phi \in [170°, 190°]$) compared with simulation and measurement. This phenomenon is similar to that in Figure 11 (a). We infer that the gap in NLOS comes from the multi-order edge diffraction at the top of cylinder, and the multi-order diffracted field component is nonnegligible for scenario 3. Combine with the conclusion of field validation, it highlights that multi-order diffraction by the top of cylinder has to be taken into account when the RX is located around the shadow boundary determined by TX and the top edge of cylinder, especially in NLOS.

The NMSE of the three scenarios are shown in TABLE 2. The predicted values of NMSE is the amplitude of the channel transfer function corresponding to UTD and CST, and the true values are measurement results. It can be seen that the error of the modified UTD model is smaller than the unmodified UTD model in the three scenarios, and there is a large gap between these two in scenario 3. Although the CST simulation results have the same trend as the measurement results, they do not show significantly higher accuracy. Considering the limited measurement points and the errors caused by the test environment, such results should be within the tolerance range.

C. CALCULATION TIME COMPARISON

Compared with CST numerical simulation, UTD calculation requires significantly less time. The comparison of time required for calculation results of the three scenarios (TABLE 1) is shown in TABLE 3 (2.3GHz Intel Core
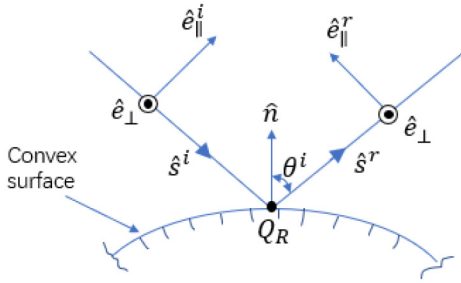
FIGURE 15. Reflection at a convex surface.

FIGURE 16. Surface diffraction at a convex surface.

i5-6300HQ CPU with 8GB RAM). We can see the huge speed advantage of UTD compared with CST numerical simulation.

V. CONCLUSION

A modified UTD model incorporating edge diffraction has been proposed for representing the field and channel when radio waves interact with a finite-length cylinder. The proposed model is validated both by simulation and measurement. The numerical results show that the modified model has higher accuracy compared to the unmodified model, when TX and RX are not at the same height - one below and the other above the top cap of the cylinder. In this case, it is crucial to incorporate the contribution of the edge diffraction to the total field.

The main error of the modified model occurs in NLOS when the receiving point is located around the shadow boundary determined by transmitting point and the top edge of cylinder. The error may stem from the multi-order diffraction which is beyond the scope of this paper but is a future work worth refining. And when transmitting point is much higher, the direct field is the main contribution of the total field, and the modified model is relatively accurate.

APPENDIX

In the Appendix, the parameters and calculation process in the equations of the reflected, diffracted and edge diffracted fields will be introduced as supplementary to Section II. Note that some parameters in the following formulas are not defined due to space limitation and can be found in [15], [16].

1) Reflected field: The unit vectors $\vec{e}_\perp$, $\vec{e}_\parallel^i$, $\vec{e}_\parallel^r$ are shown in Figure 15. $\vec{s}^i$ and $\vec{s}^r$ are the incident and reflected ray respectively, $\vec{n}$ is the surface normal at the reflection point Q_R, and

$$\vec{e}_\perp = \frac{\vec{s}^{i,r} \times \vec{n}}{|\vec{s}^{i,r} \times \vec{n}|},$$

$$\vec{e}_\parallel^{i,r} = \frac{\vec{e}_\perp \times \vec{s}^{i,r}}{|\vec{e}_\perp \times \vec{s}^{i,r}|}. \tag{18}$$

The R_s and R_h in (4) represent the scalar reflection coefficients under soft (Dirichlet) and hard (Neumann) boundary conditions respectively, calculated by:

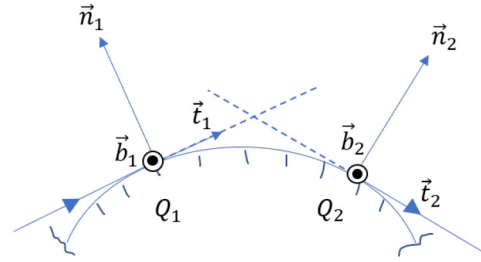$$R_{s,h} = -\left[\sqrt{\frac{-4}{\varepsilon^L}} e^{-\frac{j(\varepsilon^L)^3}{12}}\right.$$

$$\left. \cdot \left\{\frac{e^{-j(\pi/4)}}{2\sqrt{\pi}\varepsilon^L}[1 - F(X^L) + \vec{P}_{s,h}(\varepsilon^L)]\right\}\right], \tag{19}$$

in which ε^L is the Fock parameter related to the reflection field, X^L is the parameter of the transition function, $F(X)$ is the Fresnel integral, expressed as:

$$\varepsilon^L = -2m(Q_R)\cos\theta^i, \tag{20}$$

$$X^L = 2kL^L \cos^2\theta^i, \tag{21}$$

$$F(X) = 2j\sqrt{X}e^{jX}\int_{\sqrt{X}}^{+\infty} e^{-jt^2}\,dt. \tag{22}$$

in which θ^i is the angle of incident shown in Figure 15. The expression of curvature parameter m is:

$$m(Q) = \left[\frac{k\rho_g(Q)}{2}\right]^{1/3}, \tag{23}$$

in which ρ_g is the radius of curvature of the surface at Q along the direction of the incident ray. The quantities L^L, $\rho_{1,2}^r$ occurring in the above equations are given by

$$L^L = l, \tag{24}$$

$$\rho_1^r = \left[\frac{1}{l} + \frac{2\sin^2\theta_0}{\rho_\tau}\right]^{-1}, \tag{25}$$

$$\rho_2^r = l. \tag{26}$$

The Fock-Type integral function $P_{s,h}$ is defined as [33]:

$$P_{s,h}(X, q_{s,h})$$
$$= \frac{e^{-j(\pi/4)}}{\sqrt{\pi}}\iint_{-\infty}^{\infty} \frac{V'(t) - q_{s,h}V(t)}{w_2'(t) - q_{s,h}w_2(t)}e^{-jXt}dt, \tag{27}$$

and

$$q_{s,h} = \begin{cases} -j\left(\frac{ka}{2}\right)^{\frac{1}{3}}\frac{Z_s}{Z_0} & \text{TE mode} \\ -j\left(\frac{ka}{2}\right)^{\frac{1}{3}}\frac{Z_0}{Z_s} & \text{TM mode} \end{cases} \tag{28}$$

where Z_s is the surface impedance and $Z_0 = \sqrt{\mu_0/\epsilon_0}$ is for the air. In the case of PEC, $q = 0$ and $q \to \infty$ for TE and TM mode respectively.

2) Surface diffracted field: The unit vectors $\vec{b}$, $\vec{n}$, $\vec{t}$ are shown in Figure 16. $\vec{t}_1$ and $\vec{t}_2$ are tangent to the surface, $\vec{n}_1$ and $\vec{n}_2$ are the surface normal at the reflection point Q_1 and Q_2 respectively, and

$$\vec{b}_{1,2} = \frac{\vec{t}_{1,2} \times \vec{n}_{1,2}}{|\vec{t}_{1,2} \times \vec{n}_{1,2}|}. \tag{29}$$
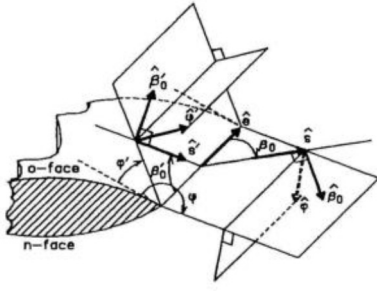
FIGURE 17. Edge diffraction at a convex surface [34].

T_s and T_h in (8) represent the scalar diffraction coefficient under soft (Dirichlet) and hard (Neumann) boundary conditions respectively, and are expressed as

$$T_{s,h} = -\left[\sqrt{m(Q_1)m(Q_2)}\sqrt{\frac{2}{k}} \right.$$
$$\left. \cdot \left\{ \frac{e^{-j(\pi/4)}}{2\sqrt{\pi}\,\varepsilon^d}\left[1 - F\left(X^d\right)\right] + \vec{P}_{s,h}\left(\varepsilon^d\right) \right\} \right]$$
$$\sqrt{\frac{d\eta(Q_1)}{d\eta(Q_2)}}\,e^{-jkt}. \tag{30}$$

The expressions of Fock parameter ε^d and parameter X^d are:

$$\varepsilon^d = \int_{Q_1}^{Q_2} \frac{m(t')}{\rho_g(t')}dt', \tag{31}$$

$$X^d = \frac{kL^d\left(\varepsilon^d\right)^2}{2m(Q_1)m(Q_2)}, \tag{32}$$

and

$$L^d = s_0, \tag{33}$$

$$\sqrt{\frac{d\eta(Q_1)}{d\eta(Q_2)}} = \sqrt{\frac{s_0}{s_0 + t}}, \tag{34}$$

$$\rho_2^d = s_0 + t. \tag{35}$$

3) Edge diffracted field: referring to Figure 17, the $\vec{\phi}'$, $\vec{\beta}_0'$, $\vec{\phi}'$, $\vec{\beta}_0$ are unit vectors in ray base coordinates

$$\vec{\phi}' = \frac{-\vec{e} \times \vec{s}'}{|\vec{e} \times \vec{s}'|}, \tag{36}$$

$$\vec{\beta}_0' = \vec{\phi}' \times \vec{s}', \tag{37}$$

$$\vec{\phi}' = \frac{\vec{e} \times \vec{s}}{|\vec{e} \times \vec{s}|}, \tag{38}$$

$$\vec{\beta}_0 = \vec{\phi} \times \vec{s}. \tag{39}$$

D_s and D_h represent the scalar edge diffraction coefficient under soft and hard boundary conditions respectively, expressed as

$$\overline{\overline{D}} = -\vec{\beta}_0'\vec{\beta}_0 D_s - \vec{\phi}'\vec{\phi}D_h. \tag{40}$$

The diffraction coefficients are given by

$$D_{s,h} = D_1 + D_2 \mp (D_3 + D_4). \tag{41}$$

The component of the diffraction coefficients are given by

$$D_1 = \frac{-e^{-j\pi/4}}{2n\sqrt{2\pi k}\sin\beta_0}\cot\left[\frac{\pi + (\phi - \phi')}{2n}\right]$$
$$F\left[kL^i a^+(\phi - \phi')\right], \tag{42}$$

$$D_2 = \frac{-e^{-j\pi/4}}{2n\sqrt{2\pi k}\sin\beta_0}\cot\left[\frac{\pi - (\phi - \phi')}{2n}\right]$$
$$F\left[kL^i a^-(\phi - \phi')\right], \tag{43}$$

$$D_3 = \frac{-e^{-j\pi/4}}{2n\sqrt{2\pi k}\sin\beta_0}\cot\left[\frac{\pi + (\phi + \phi')}{2n}\right]$$
$$F\left[kL^{rn}a^+(\phi + \phi')\right], \tag{44}$$

$$D_4 = \frac{-e^{-j\pi/4}}{2n\sqrt{2\pi k}\sin\beta_0}\cot\left[\frac{\pi - (\phi + \phi')}{2n}\right]$$
$$F\left[kL^{ro}a^-(\phi + \phi')\right]. \tag{45}$$

The distance parameter L^i associated with the shadow boundaries is given by

$$L^i = \frac{ss'}{s + s'}\sin\beta_0, \tag{46}$$

and

$$L^{ro,n} = \frac{s\left(\rho_e^{ro,n} + s\right)\rho_1^{ro,n}\rho_2^{ro,n}}{\rho_e^{ro,n}\left(\rho_1^{ro,n} + s\right)\left(\rho_2^{ro,n} + s\right)}\sin^2\beta_0, \tag{47}$$

where $\rho_1^{ro,n}$ and $\rho_2^{ro,n}$ are the principal radii of curvature of the reflected wave-front from the o- and n-faces respectively:

$$\frac{1}{\rho_e^{ro,n}} = \frac{1}{\rho_e^i} - \frac{2\left(\vec{n}_e \cdot \vec{n}_{o,n}\right)\left(\vec{s}' \cdot \vec{n}_{o,n}\right)}{|a_e \sin^2\beta_0|}. \tag{48}$$

The edge caustic ρ is given by

$$\frac{1}{\rho} = \frac{1}{\rho_e^i} - \frac{\vec{n}_e \cdot \left(\vec{s}' - \vec{s}\right)}{|a_e \sin^2\beta_0|}, \tag{49}$$

where $\vec{n}_{o,n}$ are the unit vector normal to the o- and n-faces at Q_e respectively, $\vec{n}_e$ is the unit vector normal to the edge, a_e is the radius of curvature of the edge at Q_e, for cylinder case, $a_e = r$.

REFERENCES

[1] C. De Lima *et al.*, "Convergent communication, sensing and localization in 6G systems: An overview of technologies, opportunities and challenges," *IEEE Access*, vol. 9, pp. 26902–26925, 2021.

[2] T. Wild, V. Braun, and H. Viswanathan, "Joint design of communication and sensing for beyond 5G and 6G systems," *IEEE Access*, vol. 9, pp. 30845–30857, 2021.

[3] P. S. Henry and H. Luo, "WiFi: What's next?" *IEEE Commun. Mag.*, vol. 40, no. 12, pp. 66–72, Dec. 2002.

[4] C. Lin and G. Y. Li, "Energy-efficient design of indoor mmWave and sub-THz systems with antenna arrays," *IEEE Trans. Wireless Commun.*, vol. 15, no. 7, pp. 4660–4672, Jul. 2016.

[5] J. Cuadrado and M. Á. Naya, "Editorial of special issue 'combining sensors and Multibody models for applications in vehicles, machines, robots and humans," *Sensors*, vol. 21, no. 19, p. 6345, 2021.

[6] P. Sumithra and D. Thiripurasundari, "Review on computational electromagnetics," *Adv. Electromagn.*, vol. 6, no. 1, pp. 42–55, 2017.

[7] K. Haneda *et al.*, "Chapter 2—Radio propagation modeling methods and tools," in *Inclusive Radio Communications for 5G and Beyond*, C. Oestges and F. Quitin, Eds. London, U.K.: Academic, 2021, pp. 7–48. [Online]. Available: https://www.sciencedirect.com/science/article/pii/B9780128205815000080

[8] R. F. Harrington, "The method of moments in electromagnetics," *J. Electromagn. Waves Appl.*, vol. 1, no. 3, pp. 181–200, 1987.

[9] T. Namiki, "A new FDTD algorithm based on alternating-direction implicit method," *IEEE Trans. Microw. Theory Techn.*, vol. 47, no. 10, pp. 2003–2007, Oct. 1999.

[10] T. Preston and A. Reece, "The contribution of the finite-element method to the design of electrical machines: An industrial viewpoint," *IEEE Trans. Magn.*, vol. M-19, no. 6, pp. 2375–2380, Nov. 1983.

[11] T. Weiland, "Time domain electromagnetic field computation with finite difference methods," *Int. J. Numer. Model. Electron. Netw. Devices Fields*, vol. 9, no. 4, pp. 295–319, 1996.

[12] P. Y. Ufimtsev, "New insight into the classical macdonald physical optics approximation," *IEEE Antennas Propag. Mag.*, vol. 50, no. 3, pp. 11–20, Jun. 2008.

[13] Y. Miao, Q. Gueuning, and C. Oestges, "Modeling the phase correlation of effective diffuse scattering from surfaces for radio propagation prediction with antennas at refined separation," *IEEE Trans. Antennas Propag.*, vol. 66, no. 3, pp. 1427–1435, Mar. 2018.

[14] M. Katz, *Introduction to Geometrical Optics*. New York, NY, USA: World Sci., 2002.

[15] P. Pathak, W. Burnside, and R. Marhefka, "A uniform GTD analysis of the diffraction of electromagnetic waves by a smooth convex surface," *IEEE Trans. Antennas Propag.*, vol. 28, no. 5, pp. 631–642, Sep. 1980.

[16] R. G. Kouyoumjian and P. H. Pathak, "A uniform geometrical theory of diffraction for an edge in a perfectly conducting surface," *Proc. IEEE*, vol. 62, no. 11, pp. 1448–1461, Nov. 1974.

[17] Y. Miao, J.-I. Takada, K. Saito, K. Haneda, A. A. Glazunov, and Y. Gong, "Comparison of plane wave and spherical vector wave channel modeling for Characterizing non-specular rough-surface wave scattering," *IEEE Antennas Wireless Propag. Lett.*, vol. 17, no. 10, pp. 1847–1851, Oct. 2018.

[18] S. Jiang, W. Wang, Y. Miao, W. Fan, and A. F. Molisch, "A survey of dense multipath and its impact on wireless systems," *IEEE Open J. Antennas Propag.*, vol. 3, pp. 435–460, 2022.

[19] K. Klem-Musatov, H. C. Hoeber, T. J. Moser, and M. A. Pelissier, *Classical and Modern Diffraction Theory*. London, U.K.: Soc. Explor. Geophys., 2016.

[20] P. H. Pathak, G. Carluccio, and M. Albani, "The uniform geometrical theory of diffraction and some of its applications," *IEEE Antennas Propag. Mag.*, vol. 55, no. 4, pp. 41–69, Aug. 2013.

[21] R. Tiberio, G. Pelosi, and G. Manara, "A uniform GTD formulation for the diffraction by a wedge with impedance faces," *IEEE Trans. Antennas Propag.*, vol. AP-33, no. 8, pp. 867–873, Aug. 1985.

[22] P. D. Holm, "A new heuristic UTD diffraction coefficient for nonperfectly conducting wedges," *IEEE Trans. Antennas Propag.*, vol. 48, no. 8, pp. 1211–1219, Aug. 2000.

[23] Y. Nechayev and C. Constantinou, "Improved heuristic diffraction coefficients for an impedance wedge at normal incidence," *IEE Proc. Microw. Antennas Propag.*, vol. 153, no. 2, pp. 125–132, 2006.

[24] G. Koutitas, "Multiple human effects in body area networks," *IEEE Antennas Wireless Propag. Lett.*, vol. 9, pp. 938–941, 2010.

[25] E. Plouhinec and B. Uguen, "UTD human body models comparison based on dual motion capture and radio measurements," in *Proc. IEEE/APS Topical Conf. Antennas Propag. Wireless Commun. (APWC)*, 2019, pp. 192–197.

[26] M. Mohamed, M. Cheffena, F. P. Fontán, and A. Moldsvor, "A dynamic channel model for indoor wireless signals: Working around interference caused by moving human bodies," *IEEE Antennas Propag. Mag.*, vol. 60, no. 2, pp. 82–91, Apr. 2018.

[27] Y. Miao *et al.*, "Measurement-based feasibility exploration on detecting and Localizing multiple humans using MIMO radio channel properties," *IEEE Access*, vol. 8, pp. 3738–3750, 2020.

[28] M. Peter *et al.*, "Analyzing human body shadowing at 60 GHz: Systematic wideband MIMO measurements and modeling approaches," in *Proc. 6th Eur. Conf. Antennas Propag. (EUCAP)*, 2012, pp. 468–472.

[29] E. Plouhinec, B. Uguen, M. Mhedhbi, and S. Avrillon, "3D UTD modeling of a measured antenna disturbed by a dielectric circular cylinder in WBAN context," in *Proc. IEEE 79th Veh. Technol. Conf. (VTC Spring)*, 2014, pp. 1–5.

[30] E. Plouhinec, B. Uguen, and S. Avrillon, "Comparison between a 3D UTD model and near field chamber measurements in the presence of a dielectric circular cylinder," in *Proc. IEEE/APS Topical Conf. Antennas Propag. Wireless Commun. (APWC)*, 2017, pp. 89–92.

[31] A. S. Glassner, *An Introduction to Ray Tracing*. London, U.K.: Morgan Kaufmann, 1989.

[32] Y. Miao, Q. Gueuning, M. Gan, and C. Oestges, "Adding diffuse scattering correlation to effective roughness models in ray tracing," in *Proc. 11th Eur. Conf. Antennas Propag. (EUCAP)*, 2017, pp. 828–830.

[33] L. Pearson, "A scheme for automatic computation of Fock-type integrals," *IEEE Trans. Antennas Propag.*, vol. AP-35, no. 10, pp. 1111–1118, Oct. 1987.

[34] D. A. McNamara, C. W. Pistorius, and J. Malherbe, *Introduction to the Uniform Geometrical Theory of Diffraction*. Norwood, MA, USA: Artech House, 1990.